

Randomized benchmarking of quantum gates for optimizing microwave control in ESR

Daniel K. Park^{*,a,b}, Guanru Feng^{*,a,b}, Robabeh Rahimi^{a,b}, Jonathan Baugh^{a,b,c}, Raymond Laflamme^{a,b,d,e}

^a*Institute for Quantum Computing, Waterloo, Ontario, N2L 3G1, Canada*

^b*Department of Physics and Astronomy, University of Waterloo, Waterloo, Ontario, N2L 3G1, Canada*

^c*Department of Chemistry, University of Waterloo, Waterloo, Ontario, N2L 3G1, Canada*

^d*Perimeter Institute for Theoretical Physics, Waterloo, Ontario, N2J 2W9, Canada*

^e*Canadian Institute for Advanced Research, Toronto, Ontario M5G 1Z8, Canada*

Abstract

An ensemble of electron spins with hyperfine coupled nuclei is a promising system for testing and developing ideas of quantum control and quantum error correction. We built an X-band pulsed electron spin resonance spectrometer designed for high fidelity microwave control of electron spins, including a loop-gap resonator for sub-millimeter sized samples that allows for relatively broadband control. A single-qubit randomized benchmarking protocol is employed to quantify the average errors of the Clifford gates. Improvements are achieved through phase transient correction, hardware optimization, and the design of a preparation pulse sequence to reduce inhomogeneous broadening effects. The best average fidelity for the single-qubit Clifford gates obtained here is 99.2%, limited by the T_2^* of the irradiated quartz sample.

Keywords: Electron Spin Resonance, Quantum Information Processing, Randomized Benchmarking

1. Introduction

Nuclear magnetic resonance (NMR) quantum information processors have provided excellent test-beds to develop and experimentally test quantum control techniques that can also be applied to other systems. High control fidelity has been shown in NMR quantum information processing (QIP) in the few-qubit regime [1, 2], and a scalable method for characterizing noise is well developed [3, 4, 5, 6, 7]. Quantum error correction (QEC) [8, 9, 10, 11, 12, 13] is a theory that aims to protect quantum information against the imperfections of realistic devices. The ability to implement quantum error correction is of fundamental importance for building a large scale quantum computer. Some recent experiments have realized repetitive QEC with several qubits [14, 15], but there still remain challenges for performing many cycles of QEC with large number of qubits. The major obstacle against experimental realization of multiple round QEC in NMR QIP is the difficulty in supplying highly polarized ancilla spin qubits on demand.

Moving to solid state electron spin resonance systems where an unpaired electron is hyperfine-coupled to nuclear spins is a promising path for solving this challenge. First, the electron's higher gyromagnetic ratio compared to that of nuclei can be exploited to provide about three orders of magnitude larger spin polarization, which can be transferred to hyperfine coupled nuclear spins [16, 17, 18, 19]. In addition, imbalance of the T_1 relaxation time scale between electron and nuclear spins opens the possibility for implementing open system cooling methods such as heat bath algorithmic cooling (HBAC) [20, 21, 22, 23]. HBAC can purify spin qubits beyond the thermal polarization of the bath (in this context, the electron spin's thermal polarization). Also, fast gate operations can be realized by microwave-only control when a strong anisotropic hyperfine interaction is present [24, 25, 26]. Furthermore, there is a recent proposal of building a multi-node quantum computer containing about 100 qubits employing electron and nuclear spins [27]. Engineering such system permits testing the ideas of quantum control and error correction in a setting unavailable to classical simulations, opening a path to the development of large scale quantum devices.

*These authors contributed equally to this work.

A pulsed ESR spectrometer operating at 8-12 GHz (X-band) can be constructed at relatively low cost and used as a platform for QIP experiments. At the corresponding static field (B_0) strengths, the nuclear Zeeman and hyperfine interaction terms can be comparable, allowing for universal quantum control of electron-nuclear systems to be achievable by microwave-only control [24, 25, 26]. Most available commercial pulsed ESR spectrometers do not provide the flexibility and precision of control necessary for QIP with optimal control pulses. Hence we custom-designed and built an X-band ESR spectrometer, including a variable temperature probe and specially designed loop-gap resonator (LGR). A commercial continuous flow Helium cryostat can be used to reach temperatures as low as 2 K. The challenge we focus on in this paper is to realize coherent control of the electron spin with high fidelity. While this has been accomplished in the radio frequency regime with NMR [1], it is more challenging in the microwave regime due to resonator bandwidths comparable to or narrower than control bandwidths, and the challenge of engineering ideal microwave propagation. Here, a randomized benchmarking (RB) protocol [3, 4, 5, 6, 7] is performed on a single-qubit sample in powder form, irradiated fused quartz, to characterize and improve the quality of the microwave control. Several techniques for reducing both intrinsic and extrinsic errors are applied and the benchmarking protocol quantifies the improvement gained at each step. We show that the initial RB result of $> 6\%$ error probability per gate is significantly reduced to about 0.8% after identifying and correcting several factors that cause errors in the microwave control field. The lowest error rate achieved here is of the same order as inhomogeneous dephasing in the irradiated quartz sample we use (T_2^*).

2. Instrumentation

2.1. X-band pulsed ESR Spectrometer

A schematic of the home-built X-band pulsed ESR spectrometer is depicted in Fig. 1. The microwave source (Rohde and Schwarz SMF100A) can provide a continuous wave (CW) output ranging from 1 to 22 GHz, and is typically operated at $\omega_0 \sim 10$ GHz for our applications. The source is equipped with enhanced phase noise performance and high output power up to +25 dBm. In order to generate arbitrary pulse shapes such as GRAdient Ascent Pulse Engineering (GRAPE) pulses [28], we use a single-sideband (SSB) up-conversion technique [29, 30] with an I-Q modulator as

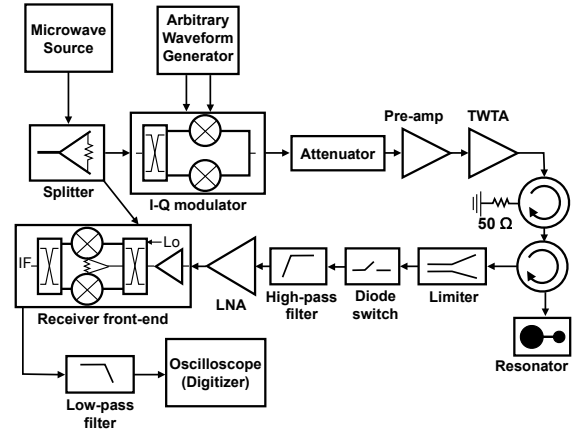


Figure 1: Schematic of the home-built X-band ESR spectrometer. A signal generated from the microwave source is mixed at the I-Q modulator with 0° and 90° phase-shifted components of a shaped pulse from the arbitrary waveform generator. The I-Q modulator outputs the shaped pulse at upconverted frequency, and the pulse phase is accurately controlled (see text). A TWT amplifier combined with a pre-amplifier and an attenuator provides a pulse output power up to 500 W. The amplified pulse is transmitted to the loop-gap resonator containing the sample. In the receiver, the ESR signal is mixed with the reference frequency and downconverted to an IF signal, which is digitized by a fast oscilloscope.

the SSB mixer. A 1.2 GS/s Tektronix arbitrary waveform generator (AWG) provides both 0° and 90° phase-shifted pulse inputs from two output channels with intermediate frequency (IF) ω_{IF} ranging from 150-400 MHz. Applying IF signals of same amplitude but phase-shifted by $\pi/2$ at I and Q ports suppresses the phase error of the output pulse due to the I-Q modulator's non-linear power response. The phase of the output microwave pulse is then controlled by the phase of IF signal generated by AWG, accurate upto 1 part in 16384. As the CW microwave signal with frequency ω_0 is mixed with the IF inputs with frequency ω_{IF} at I and Q ports, the I-Q modulator outputs only the upconverted signal at $\omega_0 + \omega_{IF}$, and the lower sideband is suppressed. The shaped pulse must be amplified prior to being launched to the resonant sample cavity. A traveling wave tube (TWT) amplifier with maximum output power ~ 1 kW is employed. Prior to the TWT, a variable attenuator and a low-gain solid-state amplifier are used in order to fully utilize the dynamic range of the TWT. The output microwave pulse from the TWT amplifier is directed by a circulator and travels to the loop-gap resonator (see Sec. 2.2) that surrounds the sample,

where the pulse results in an oscillating magnetic field \mathbf{B}_1 . The circulator has a peak power limit of 500 W, hence the TWT input is adjusted so that its output will not exceed this value. The spin signal is directed by the circulator to a low-noise preamplifier and then to the receiver, where it is mixed with the reference frequency ω_0 and downconverted to ω_{IF} . The receiver includes a second stage of low-noise amplification. A diode switch (Advanced Technical Materials S1517D) is used to protect the receiver from being damaged by high power pulses from circulator leakage and reflection of signals from the loop-gap resonator. The switch is controlled by a marker channel of the AWG. In addition, a diode limiter is used to protect the switch, which is also easily damaged by high microwave power. After the switch, a high-pass filter is incorporated in order to remove switching transients. Finally, the spin signal is digitized using a fast LeCroy oscilloscope and is recorded on a computer for further data processing.

2.2. Loop-gap resonator

We designed a loop-gap resonator (LGR) adapted from [31] with a resonance frequency of about 10 GHz. The LGR is a lumped element resonant circuit with inductance and capacitance determined by its geometry. The advantages of the LGR compared to conventional cavity resonators in commercial spectrometers is a larger filling factor, large $\|\mathbf{B}_1\|$ per square root watt, good \mathbf{B}_1 uniformity over the sample volume and larger control bandwidth (and shorter pulse ringdown times) due to a lower quality factor Q [30, 32]. Figure 2 shows a schematic of the two-loop, one-gap resonator we employ. The loops and the gap are cut by wire electric discharge machining from a 9.6 mm \times 5.4 mm \times 2.5 mm copper block. The loop radii are 1.2 mm and 0.6 mm, and the gap is 0.1 mm wide and 3 mm long. The geometry of the LGR was chosen for a 10 GHz resonance frequency and $Q \sim 250$. The microwave electric field is the strongest in the gap while the magnetic field is the strongest in the sample loop.

2.3. Variable temperature probe

The resonator is placed in a copper rectangular box of dimensions 9.4 mm \times 9.6 mm \times 5.4 mm. The lowest resonance frequency of the box is well above 12 GHz, and hence does not interfere with the desired resonance. The inner conductor of a coaxial cable is formed into a one-turn loop and brought close to the larger of the two LGR loops, where it inductively couples the microwave signal to the LGR. The outer conductor of the coaxial cable is copper, and the inner conductor is silver-plated

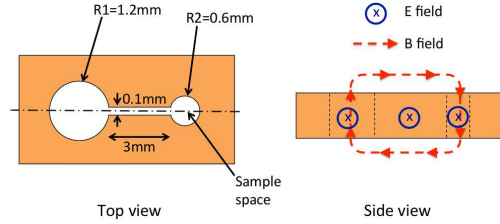


Figure 2: Schematic of the loop-gap resonator. The resonator has two loops and one gap, and it is made of copper. The geometry of the resonator is determined to yield about 10 GHz resonance frequency with $Q \sim 250$. The magnetic and electric field directions are shown in the side view. The electric field is the strongest in the gap while the magnetic field is the strongest in the loop, and the sample is placed inside the smaller loop.

copper. Impedance matching to the resonator is done by adjusting the position of the LGR relative to the coupling inductor.

The $\mathbf{B}_1(t)$ control field seen by the sample does not exactly match the desired pulse shape due to nonlinearities in the pulse generation and amplification, and due to the finite bandwidth ($\sim \omega_0 / (2\pi Q)$) of the resonator. In order to detect and correct these errors, we insert a second, smaller diameter coaxial cable terminated with an inductive loop as a pickup coil, as shown in Fig. 3. This pickup coil measures the microwave field in the vicinity of the sample. Systematic pulse errors are reduced substantially by comparing the pulse measured by the pickup coil with the desired pulse, and adjusting the input waveform to minimize the difference between the two. However, this procedure assumes that the transfer function of the pickup coil is flat over the entire bandwidth of the control field, which is only approximately true in practice. It also assumes that the pickup coil only couples to the resonant mode and does not itself introduce new modes.

The rectangular box containing the resonator is held inside a cylindrical probe-head made of copper, with 28 mm inner diameter and 85 mm inner depth. A schematic of the probe is illustrated in Fig. 3. It is designed to fit into the Oxford Instruments CF9350 continuous-flow cryostat, and can be cooled to ~ 2 K by pumping on the Helium space. While low temperature is required for reaching high electron spin polarizations, this work focuses on characterizing the precision of spin manipulations via the microwave control field, and as a first step this is done at room temperature.

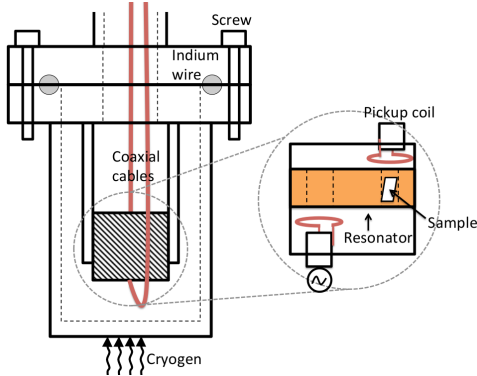


Figure 3: Schematic of the custom-built ESR probe. The two-loop, one-gap resonator is placed in a copper rectangular box, and the box is placed in a cylindrical copper enclosure which makes contact with liquid helium vapour during cryogenic cool down. The cylindrical enclosure is sealed using indium wire and screws, and is evacuated during experiments. The inner conductor of a coaxial cable at one end is used to create an inductive loop, and the loop is placed near the larger LGR loop in order to couple the microwave input to the LGR. Tuning and matching of the resonance can be done by adjusting the position of the LGR relative to the coupling inductor. A second coaxial cable is used to detect the microwave field during a pulse in order to adjust the input waveform to compensate for systematic errors in the control field.

3. Single-qubit randomized benchmarking protocol

Randomized benchmarking (RB) [3, 4, 5, 6, 7] is a scalable approach to estimate average error probabilities of quantum gate operations apart from the state preparation and measurement (SPAM) errors. RB protocols have been used to assess average gate fidelity in various quantum information processors such as trapped ions [4, 33, 34], liquid state NMR [1], superconducting qubits [35, 36], atoms in optical lattices [37], and ^{31}P donor in silicon [38]. The strategy of RB is to randomize over a set of computational gate sequences followed by a reverse (recovery) operation so that the entire evolution is the identity operation in the absence of error. The computational gate set should be chosen such that it forms a depolarizing channel upon averaging, which can be true as long as the errors are mostly gate-independent [3, 6, 7]. The depolarizing parameter p of the averaged channel $\bar{\Lambda}$ is given by:

$$\bar{\Lambda} = (1 - p)\rho + \frac{p}{D}\mathbb{1} \quad (1)$$

and can be related to the average gate fidelity. Here D is the dimension of ρ . Randomization over the full unitary group provides a benchmark over the complete set of quantum gates. However, since the unitary group is a continuous set with a number of parameters increasing exponentially in the number of qubits n , generating an arbitrary unitary operator is also exponentially hard with increasing n . Therefore, it is more practical to benchmark a discrete set of gates. It is desirable that the operations can be efficiently simulated and can be generated from a small set of elementary one and two qubit gates. The Clifford group, denoted as C , is one such set that is attractive for benchmarking for several reasons. First, a universal gate set can be generated using C with the help of a magic-state and measurement in the computational basis, which means that there exists a universal quantum computation model in which all necessary gates can be drawn from the Clifford group [39]. Furthermore, benchmarking the Clifford gates is useful since most encoding schemes for fault tolerant QIP are based on stabilizer codes, in which the error correction is performed using Clifford gates.

We followed the single-qubit randomized benchmarking protocol implemented in the liquid state NMR benchmarking experiment presented in [1]. The single-qubit Clifford randomization is equivalent to a randomization using the 48 operations parametrized as [1, 40, 41]

$$SP = \exp\left(\pm i\frac{\pi}{4}Q\right)\exp\left(\pm i\frac{\pi}{2}V\right), \quad (2)$$

$$Q \in \{\sigma_x, \sigma_y, \sigma_z\}, V \in \{\mathbf{1}, \sigma_x, \sigma_y, \sigma_z\}.$$

In this protocol, the $\pi/2$ rotations (which belong to the symplectic group and are denoted as S in Eq. 2) are computational operations while the Pauli operations (which belong to the Pauli group and are denoted as P in Eq. 2) serve only to toggle the Pauli frame which depolarizes the noise. SP realizes an operation in the Clifford group. To quantify the average error per gate, randomly chosen sequences of L Clifford operations in Eq. (2) are applied to a fixed known initial state. A natural choice for the initial state is the thermal state, which can be simply written as $\rho_i = \sigma_z$ since the identity part of the density matrix is irrelevant in both unitary evolution and the measurement.

The initial state is tracked through a sequence of Clifford operations (Eq. 2), and the sequence is truncated at different lengths $l \leq L$ to measure the fidelity decay curve. At each truncation l , a recovery gate is chosen at random to return the state to either $\pm\sigma_z$. Then a read-out pulse sequence, which contains a $\pi/2$ rotation pulse, a 700 ns delay and a π rotation pulse, is used to

form a spin echo. The amplitude of the spin echo in the time domain, equivalent to the integrated intensity of the corresponding absorption peak in the frequency domain, is the quantity measured. In the experiment, we pre-calculate the final state prior to the spin echo measurement, and choose the phase of the $\pi/2$ read-out pulse so that we always measure the positive eigenvalue. The quantum circuit implementing a particular series of Clifford operations is shown in Fig. 4.

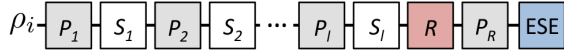


Figure 4: A particular realization of Clifford sequence in the randomized benchmarking protocol. P and S indicate Pauli and computational operations, respectively, and R is the recovery gate that brings the state to either $+\sigma_z$ or $-\sigma_z$ at random with equal probabilities. The sequence is truncated at some length l , and the final state is measured by the amplitude of the electron spin echo after a read-out pulse sequence (see text). The electron spin echo measurement part is denoted ESE in the figure.

The single-qubit RB protocol can be summarized as follows [1]:

1. Choose a maximum number of Clifford operations L , and a set of random integers $l = \{l_1 < \dots < L\}$ that is the length of a truncated pulse sequence (i.e. a subsequence). The number of elements in l is denoted N_l .
2. Generate N_g random sets of L computational gates, and truncate each sequence at length $l_k \in l$.
3. For each subsequence of length l_k (total $N_g \times N_l$ subsequences), do the following:
 - (a) Generate N_p random sets of Pauli gates of length $l_k + 2$.
 - (b) Interleave computational gates with the $l_k + 1$ Pauli gates.
 - (c) Calculate recovery operation and insert it after $(l_k + 1)^{th}$ Pauli gate.
 - (d) Insert final Pauli randomization gate before the spin echo detection.
 - (e) Calculate the phase of the spin echo read-out pulse that yields the positive eigenvalue of σ_z .
4. Evolve the known initial state under each of the $N_g \times N_l \times N_p$ number of random pulse subsequences.
5. Measure the electron spin echo amplitude at the end of each subsequence and compare with the same measurement on a reference state.

6. For each l_k where $k = 1 \dots N_l$, calculate the average remaining spin magnetization along σ_z by averaging over $N_g \times N_p$ subsequences.
7. Plot the average remaining signal as a function of l , and fit the curve to $f_l = \alpha(1 - p)^l$, where the average gate error is $p/2$. The state preparation and measurement (SPAM) error is absorbed in the constant α .

As indicated in steps 6 and 7, we calculate the average gate error from the decay rate of $\langle \sigma_z \rangle$ as a function of the number of gates l .

4. Simulations and initial experimental results

The single-qubit system employed for the benchmarking experiment is irradiated fused quartz [42], a paramagnetic sample in powder form. We measured $T_1 = 160 \mu\text{s}$, $T_2 = 5 \mu\text{s}$, and $T_2^* = 60 \text{ ns}$ at room-temperature. T_2^* is determined from the linewidth of the thermal-state ESR spectrum in the frequency domain. The T_2^* line-broadening here is mainly due to the anisotropy of the g -value, which produces a powder pattern of width of about 5 MHz, and also to non-uniformity of the static magnetic field. Different spins within the sample may also experience different nutation frequencies due to the inhomogeneity of the applied microwave field (\mathbf{B}_1) in the resonator loop. To obtain the \mathbf{B}_1 distribution profile, we measure the time-domain Rabi oscillations. Simulations indicate that T_2^* in this spin system does not contribute significantly to the Rabi decay envelope, rather it is dominated by \mathbf{B}_1 inhomogeneity. Therefore, the Fourier transform of the time-domain Rabi oscillations is a good estimate of the \mathbf{B}_1 distribution profile over the sample. This distribution is confirmed by comparing experimental and simulated decays, which allows us to refine the estimate for the \mathbf{B}_1 distribution profile. The ESR line-broadening due to T_2^* , as well as the \mathbf{B}_1 distribution profile, are shown in Fig. 5. Using the decoherence parameters and the \mathbf{B}_1 inhomogeneity data, we simulated a RB protocol with $N_g = 7$, $N_p = 14$ giving a total of 98 sequences, and $l = \{1, 2, 7, 9, 10, 12, 14, 18, 20, 21, 25, 28, 32, 57, 60, 66, 74, 97, 110, 128\}$ chosen at random. Both computational and Pauli gates are realized by 35 ns long Gaussian-shaped microwave pulses, yielding Clifford operations that are 70 ns in total length. Figure 6 summarizes the simulation results under four different conditions: (1) no \mathbf{B}_1 inhomogeneity and no T_2^* effect, (2) with \mathbf{B}_1 inhomogeneity and no T_2^* effect, (3) no \mathbf{B}_1 inhomogeneity and with T_2^* effect, (4) with \mathbf{B}_1 inhomogeneity and T_2^* effect. T_1 and T_2 processes are included

in all four simulations by using a Lindblad model. In the absence of any local field inhomogeneities, the simulated error per gate is 0.37%. Since there are no control field errors in this simulation, the imperfection is solely due to T_1 and T_2 processes. When the local field inhomogeneities are included, the error per gate increases to 0.45% for B_1 , 1.08% for T_2^* and 1.18% for both B_1 and T_2^* . We conclude from these simulations that the T_2^* effect should contribute more significantly to the error rate than the B_1 inhomogeneity does.

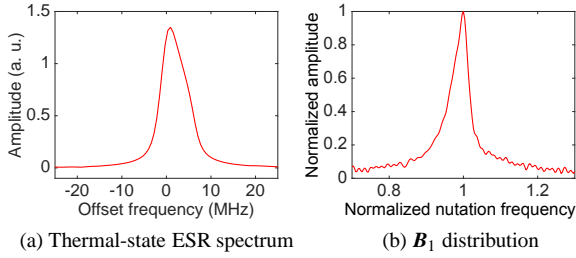


Figure 5: (a) Thermal-state ESR spectrum of irradiated fused quartz obtained by Fourier transforming the spin echo signal. The linewidth is mainly determined by the anisotropy of the g-value and inhomogeneity of the static magnetic field. The asymmetric line shape indicates the powder pattern of the quartz sample. (b) B_1 distribution profile obtained by taking the Fourier transform of the Rabi oscillation data (see text). The nutation frequency is normalized by the peak frequency of the distribution.

Without any optimization of the microwave pulses beyond simple power calibrations, RB was implemented experimentally in the quartz single-qubit system. The error per gate was $\sim 6\%$, indicating an insufficient level of control for QIP tasks. In the following section, we discuss the modifications to the hardware configuration and to pulse shaping techniques that allow for significant reductions in the error rate.

5. Pulse optimizations

The pickup coil introduced in Sec. 2.3 is used to directly measure the microwave field in the vicinity of the sample. The largest and most obvious pulse imperfection revealed by the pickup coil was a phase transient error. The input pulse is 35 ns Gaussian shape applied along the rotating frame y-axis, meaning that the amplitude of the imaginary component (x-axis component) of the pulse is zero. However, as shown in Fig. 7a, the measured output pulse indicates a noticeable phase transient

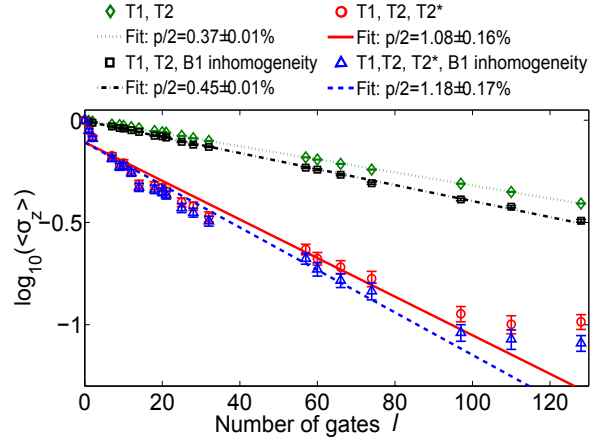


Figure 6: Results of simulated randomized benchmarking on the single-qubit (fused quartz) spin system plotted in semi-log scale. The expectation value $\langle \sigma_z \rangle$ is measured after application of l randomized gates and fitted using $f_l = \alpha(1-p)^l$. The expectation value $\langle \sigma_z \rangle$ for each value of l is the result averaged over $N_g \times N_p = 98$ random sequences. The simulations use experimentally measured values of T_1 , T_2 , and T_2^* at room-temperature, which are 160 μs , 5 μs , and 60 ns, respectively. Green (\diamond) is obtained by simulating with only T_1 and T_2 of the electron as the error source. Black (\square) includes B_1 field inhomogeneity. Red (\circ) shows the simulation result with T_2^* , but no B_1 distribution, and blue (\triangle) is the result from simulating all noise sources, T_1 , T_2 , T_2^* and B_1 distribution. The size of the error bars represents standard error of the mean averaged over the 98 sequences.

with nonzero imaginary component. The transient effect leads to undesired spin dynamics as shown in Fig. 7b.

Figure 7b shows the rotation of the spin magnetization vector as the power of the input Gaussian pulse is varied. The pulse is applied along the y-axis to the spin state σ_z , and it is followed by a 700 ns delay and a π pulse to form an echo. The solid and dashed curves represent real (x) and imaginary (y) components of the measured spin echo amplitude. In the absence of the pulse error, the imaginary part should be zero for all powers as the spin magnetization vector remains within the x-z plane. However, the nonzero y-component in Fig. 7b indicates that the spin is rotated out of the x-z plane by the phase transient. In order to suppress this pulse error, we designed an input pulse with an imaginary part of equal amplitude but opposite sign to cancel the transient. The phase transient corrected (PTC) pulse is designed as follows. First, we take the imaginary

part of the measured pulse shape, and digitize it so that the time resolution of the measured pulse matches the AWG sampling rate. Then we multiply the imaginary part of the digitized pulse by a factor of -1 to negate the phase error. However, the digitization step can introduce small unwanted scaling in the pulse amplitude, and thus the multiplication by -1 may not exactly cancel the unwanted imaginary component. We find that introducing a scaling factor of 1.07 to the PTC pulse yields the best result in minimizing the phase transient effect. Figure 8a demonstrates that using the modified input pulse, the phase transient error is significantly reduced. As shown in Fig. 8b, the deviation of the spin evolution trajectory from the x-z plane is significantly suppressed when the same experiment is conducted using the PTC input pulse. It should be noted that the real component of the pulse is asymmetric in time, with a slowly decaying tail; this is due to the finite bandwidth of the resonator. However, since the integrated pulse area can be calibrated with high accuracy to yield the desired spin rotation, we only need to correct the distortion in the imaginary part of the pulse.

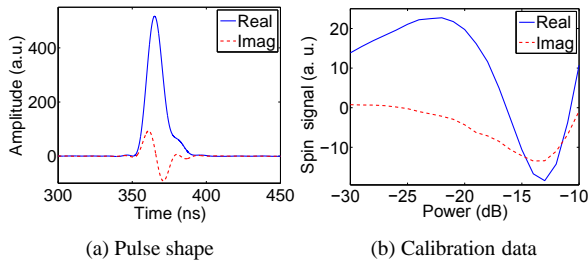


Figure 7: (a) The shape of a 35 ns Gaussian pulse measured using the pickup coil shown in Fig. 3. The pulse is applied along the rotating frame y-axis. The solid curve represents the real part (y-axis component) of the measured pulse and the dashed curve is the imaginary part (x-axis component). Ideally, the imaginary component of the pulse is zero, however the pickup coil reveals a large phase transient. (b) Spin magnetization signal measured as a function of the pulse power of the 35 ns Gaussian pulse shown in (a). The Gaussian pulse is applied along the y-axis to the spin state σ_z , and is followed by a 700 ns delay and a π pulse to form an echo. Without pulse imperfections, only the real part (x component, solid curve) of the spin signal should oscillate as a function of the pulse power while the imaginary part (y component, dashed curve) should be zero. However, the phase transient leads to an undesired spin rotation out of the x-z plane.

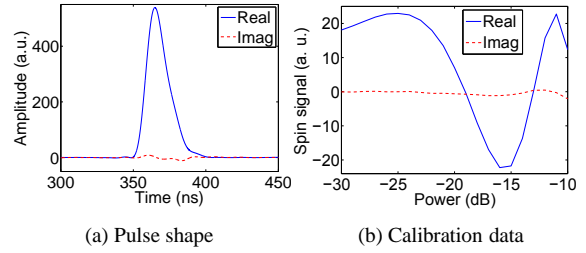


Figure 8: (a) The shape of a 35 ns Gaussian pulse after implementing the phase transient correction explained in the text. The unwanted imaginary component (x-axis component, dashed curve) of the pulse is suppressed. (b) Spin magnetization signal measured as a function of the pulse power of the corrected pulse. The deviation of the spin trajectory from the x-z plane (dashed curve) is much reduced compared to the uncorrected pulse.

Another significant contribution to the gate error was the phase and amplitude droop of the TWT microwave amplifier. We found this error to be strongly dependent on the amplifier unblanking time delay. Figure 9a shows the shape of a series of phase transient corrected 35 ns Gaussian pulses when the TWT unblanking delay is set to 300 ns. It is clear from the figure that both amplitude and phase are unstable until about $2 \mu\text{s}$ after the blanking is turned off (at $t=0$ in Fig. 9a). Figure 9b shows that when we use a $2 \mu\text{s}$ unblanking time instead of 300 ns, the stabilities of pulse amplitude and phase are very good.

After the phase transient effect is corrected and the TWT unblanking delay is set to $2 \mu\text{s}$, the randomized benchmarking experiment was carried out again, and the error per gate found to be $1.72 \pm 0.25\%$. This error rate is still about an order of magnitude larger than the rate expected solely from T_1 and T_2 processes. A large part of this remaining error is due to ensemble inhomogeneity effects, which we demonstrate in the next section.

6. Selection sequence to reduce local field inhomogeneities

The simulation results shown in Fig. 6 indicate that the average gate fidelity is limited by local field inhomogeneities: the static distribution of Larmor frequencies (T_2^*) and the inhomogeneity of the microwave field \mathbf{B}_1 across the sample volume. The \mathbf{B}_1 distribution has relatively narrow width and we observed from simulations that T_2^* effect contributes more strongly to the error rate.

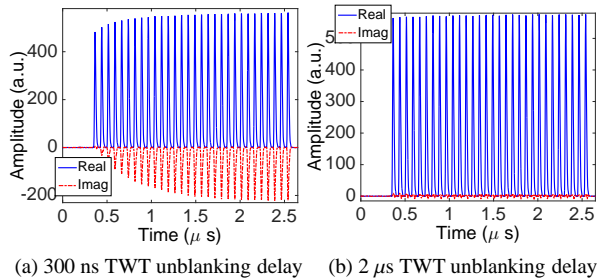


Figure 9: (a) Series of the phase transient corrected 35 ns Gaussian pulses with 300 ns TWT unblanking delay. Here $t = 0$ corresponds to when the unblanking occurs. The amplitude and phase of the pulse require about 2 μ s to stabilize after unblanking. (b) The same series of pulses with a 2 μ s unblanking delay, indicating good stability of both phase and amplitude. Here unblanking occurs at $t = -1.7 \mu$ s with respect to the time axis on this plot.

To test this experimentally, we designed a protocol to effectively narrow the static field distribution.

One approach to overcome such field inhomogeneity is to use composite pulses [43]. However, useful composite pulses are typically much longer than the lengths of the base pulses. Given the timescales of T_2^* and T_2 in our system, composite pulses do not improve gate fidelities, but rather worsen them. For example, at least three individual pulses are required for the spin inversion (π -rotation) composite pulse that is robust to the T_2^* field inhomogeneity [44], meaning that the total pulse duration of either a Pauli or a computational gate is $3 \times 35 \text{ ns} = 115 \text{ ns}$. A simulation using the 115 ns composite pulses shows that even in the absence of the field inhomogeneities, where the error solely comes from T_1 and T_2 processes, the error per gate would become $1.08 \pm 0.01\%$. Thus, use of composite pulses does not improve the average gate fidelity in this ESR system.

Another approach is to design a pulse sequence to select a subset of the spin ensemble within a narrower static field distribution, similar to the idea of RF selection in NMR QIP [1, 45, 46]. The selection sequence we use is constructed as follows. First, a 400 ns GRAPE pulse with 1 ns discrete time step rotates spins that experience exactly on-resonance local field by 2π around the x-axis, with a calculated unitary fidelity (Hilbert-Schmidt (HS) norm) of 99.9%. For the spin packets that experience off-resonance local fields, the unitary fidelity quickly decreases with offset. Hence mostly on-resonance spin are left pointing along the z-axis after

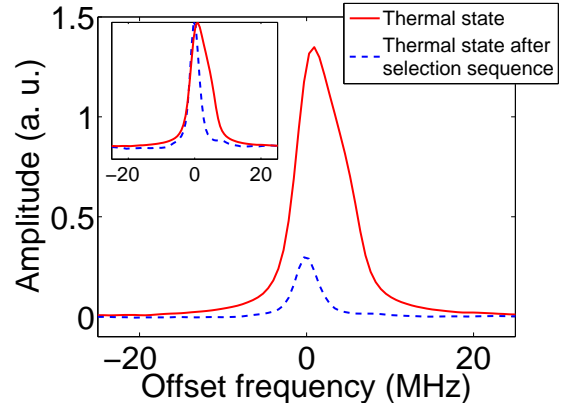


Figure 10: Comparison of the ESR spectra before (solid) and after (dashed) applying the selection sequence explained in the text. The signal intensity is substantially reduced since only a small portion of the spin magnetization remains after the sequence. However, the linewidth is significantly reduced, as shown in the inset where we plot the two spectra normalized to the same amplitude. The sequence reduces spin magnetizations at larger frequency off-sets while selecting spin packets near zero off-set frequency. Hence the center of the ESR spectrum shifts towards zero off-set frequency after the selection sequence.

the GRAPE pulse. Next, we wait for a duration $\sim T_2$ in order to dephase the transverse component of the off-resonance spin packets pointing along other directions in the Bloch sphere. By repeating these two steps, an initial state can be prepared that effectively corresponds to a narrowed ESR linewidth. Ideally, the dephased off-resonance spin packets will be in a fully unpolarized state and not contribute to subsequent spin signals. Although longer wait time is desired for eliminating the transverse spin magnetization, the delay must be short compared to T_1 in order to minimize the repolarization of off-resonance spins. We find that repeating the sequence four times and using a delay equal to T_2 provides the best narrowing of the ESR linewidth while retaining a signal level well above the noise. Under these conditions, T_2^* is extended to more than twice its original length, as shown in Fig. 10. Note that the selection sequence does not necessarily improve the \mathbf{B}_1 field homogeneity. In order to reduce \mathbf{B}_1 field inhomogeneity, spin packets from localized region of the sample need to be selected. We do not see any significant improvement in the \mathbf{B}_1 distribution after this sequence. Nevertheless, since the dominant source of error is the T_2^* process, we show in the next section that this selection sequence

does indeed improve the average gate fidelity.

7. Results and discussion

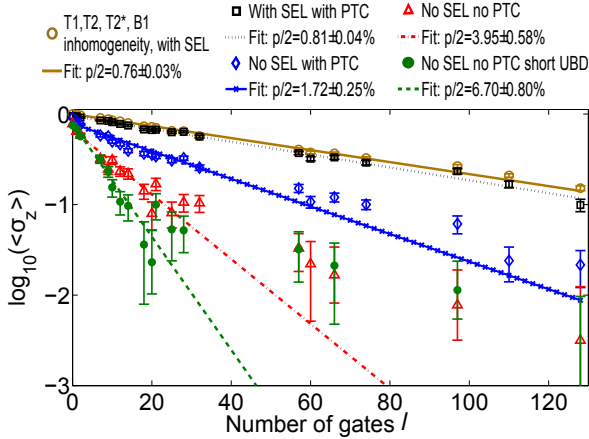


Figure 11: Summary of experimental results plotted in semi-log scale. The expectation value $\langle \sigma_z \rangle$ is measured after l randomized gates and fitted using $f_l = \alpha(1 - p)^l$. The expectation value $\langle \sigma_z \rangle$ for each value of l is the result averaged over $N_g \times N_p = 98$ random sequences. Before incorporating the improvements explained in the text, the average error rate is above 6% (\bullet). The triangles (Δ) indicate the result obtained after setting the TWT unblanking delay to $2 \mu\text{s}$, and the error probability is reduced to 3.95%. Using the phase transient corrected pulses, the error rate is further reduced to 1.72% (\diamond). Finally, after incorporating the selection sequence for increasing T_2^* , the error per gate is decreased to 0.81% (\square). The open circles are the results of the RB simulation that should be compared to the latter experimental data: it includes the selection sequence, the experimental T_1 , T_2 , T_2^* values, and the experimental B_1 inhomogeneity profile, but otherwise assumes perfect pulses. The size of the error bars represents the standard error of the mean averaged over the 98 sequences. In the plot legend, SEL, PTC and UBD stand for the ‘selection sequence’, ‘phase transient corrected’, and ‘unblanking delay’, respectively.

Randomized benchmarking experimental results under different conditions are plotted in Fig. 11. The semi-log plot shows the expectation value of σ_z measured after applying l Clifford gates. The depolarizing constant as well as the error per gate can be calculated from the decay rate of the expectation value as a function of the number of Clifford operations. The initial experimental RB data, without any improvements, is

plotted (\bullet symbol) and corresponds to an error probability of 6.7%. Changing the TWT unblanking delay (Δ symbol) results in an error probability of about 4%. Both of these give decay curves that deviate substantially from a single-exponential fit after about 30 gates. Hence, we only use the first few points to fit to an exponential and extract the error rate. Further control improvement is achieved by employing phase transient corrected pulses (\diamond symbol). Combining the longer unblanking delay with phase transient corrected pulses, the error per gate is reduced to $1.72 \pm 0.25\%$. However, the non-exponential behaviour of the decay curve is still observed. This non-exponential behaviour can be explained by the T_2^* field distribution over the spin ensemble which is a form of incoherent error (see Appendix). Note that incoherent error is not restricted to spatial ensemble systems [49], but applies to single quantum systems when a parameter (e.g. local field) fluctuates between the many experiments that must be averaged to measure an observable. The non-exponential decay here is understood as a sum of single-exponential decay curves with different decay rates for different spin packets. The Appendix shows in detail how incoherent error can result in a non-exponential decay. After incorporating the selection sequence to increase T_2^* as described above, the decay curve fits well to a single-exponential curve.

With the selection sequence, the error per gate is reduced to $0.81 \pm 0.04\%$. This is nearly an order of magnitude improvement compared to the initial result of 6.7%. Simulation of the RB protocol with the selection sequence using experimentally determined values of T_1 , T_2 , T_2^* and the B_1 distribution is also shown in Fig. 11 (\circ symbol). The simulated error per gate is $0.76 \pm 0.03\%$. The strong agreement between the simulation and experimental results suggests that the error due to microwave control imperfections has been reduced to the same order as the intrinsic error ensemble dephasing, i.e. the precision of control is limited by T_2^* .

8. Conclusions and future work

We built an X-band pulsed ESR spectrometer, including variable temperature probe with a loop-gap resonator, for QIP applications that require very accurate spin manipulations. The randomized benchmarking protocol of the single-qubit Clifford gate operations was employed to characterize and improve the quality of microwave control. The initial benchmarking yielded about 93% average single-qubit Clifford gate fidelity. Several improvements to the control were discussed, such as the pulse phase transient correction method,

stabilization of the microwave amplifier, and a selection pulse sequence to reduce the inhomogeneous line-broadening. These strategies allowed us to reduce the error rate by an order of magnitude to obtain an average fidelity of 99.2%. The simulation results show that this level of precision is limited by the T_2^* of the irradiated quartz sample. In a sample with longer T_2^* , T_2 and T_1 values, the extrinsic errors due to microwave imperfections could again dominate. We expect that a suitable solid-state microwave amplifier should outperform the TWT amplifier in both noise figure and amplitude/phase stability, and it would be interesting to use RB for a side-by-side comparison of these amplifier technologies in the context of quantum control. It would also be interesting to use RB to characterize microwave control in multi-qubit systems, i.e. an electron spin coupled to one or more nuclear spins [18, 19, 24, 25, 26]. If gate fidelities similar to those reported in this work can be achieved, then such hybrid electron-nuclear spin systems could be ideal for testing quantum algorithms such as heat bath algorithmic cooling [20, 21, 22, 23] and quantum error correction [8, 9, 10, 11, 12, 13], in particular, multiple-round quantum error correction.

Acknowledgements

This research was supported by NSERC, the Canada Foundation for Innovation, CIFAR, the province of Ontario and Industry Canada. We thank David Cory and Troy Borneman for providing the single-qubit sample, Colm Ryan, Yingjie Zhang and Jeremy Chamilliard for their contributions to the spectrometer, and Roberto Romero and Hiruy Haile for help with machining.

Appendix A. Effect of incoherent error on the fidelity decay

Incoherent error of a quantum process can be caused by classical noise, for example, a distribution over external experimental parameters [47, 48] such as \mathbf{B}_1 inhomogeneity and T_2^* line-broadening. In our system, after optimizing the TWT unblanking delay and using the phase transient corrected pulses, T_2^* effect remains as the dominant source of the incoherent error. \mathbf{B}_1 inhomogeneity is also present, but does not critically reduce the control fidelity at current level. Hence only the T_2^* noise is considered in our incoherent error discussions. In this section, we adapt the analysis presented in [1] that was used to describe \mathbf{B}_1 inhomogeneity effect on the fidelity decay to explain how T_2^* gives rise to the non-exponential decay observed in our experimental (Fig. 11) and simulated (Fig. 6) results.

Due to T_2^* local field inhomogeneity across the sample, unitary errors with different strengths arise on the spins experiencing off-resonance fields. Intuitively, since the spins at different Larmor frequencies experience different average unitary errors, the signal decay curve should contain multiple depolarization rates, which explains the non-exponential behavior. For more concrete analysis, we consider a single step which consists of a computational gate (S) followed by a Pauli gate (P) in a randomized benchmarking sequence. The superoperator describing the process can be expressed as:

$$\hat{\Lambda} = \int d\epsilon g(\epsilon) \hat{\Lambda}_\epsilon PS. \quad (\text{A.1})$$

Here ϵ is off-resonance frequency, $\hat{\Lambda}_\epsilon$ is the superoperator describing the cumulative error of PS for the fraction of the system with off-resonance frequency ϵ , and $g(\epsilon)$ is the distribution of ϵ . $g(\epsilon)$ can be obtained from a frequency domain thermal state spectrum (Fig. 5a for example). For a given ϵ , the cumulative error strength of this single step can be calculated by

$$\xi = 1 - \frac{1}{4} |\text{Tr}(S P U_{inh}^\dagger)|^2, \quad (\text{A.2})$$

where U_{inh} is the faulty implementation of S and P due to the local field inhomogeneity, and $\frac{1}{4} |\text{Tr}(S P U_{inh}^\dagger)|^2$ is the gate fidelity (Hilbert-Schmidt (HS) norm) of the faulty implementation. As the off-resonance fields cause undesired rotations along z-axis, which don't commute with rotations along x-axis or y-axis, the error strength ξ is different for different combinations of S and P . It can be easily verified that for a given ϵ there are 9 different error strengths depending on different cases of S and P (e.g. whether S and P are rotations along z-axis, they are along parallel or anti-parallel axes, or the rotation axis of S is clockwise or counterclockwise from that of P). The 9 types are labelled from 1 to 9 in Tab. A.1.

Therefore, for a fixed ϵ , the error is gate-dependent. However, it is proven in [3, 6, 7] that the cumulative effect of the gate-dependent errors in the randomized benchmarking can still be described as a depolarizing channel as long as the gate dependence is weak. Therefore, for the spin packet with the off-resonance frequency ϵ , upon averaging over random gate sequences, $\hat{\Lambda}_\epsilon$ in Eq. A.1 forms a depolarizing channel $\hat{\Lambda}_{\epsilon,ave}$ with the depolarizing factor p_ϵ . $\hat{\Lambda}_{\epsilon,ave}$ and p_ϵ can be ex-

$P \backslash S$	X90	-X90	Y90	-Y90	Z90	-Z90
X180	1	3	4	2	7	7
-X180	3	1	2	4	7	7
Y180	2	4	1	3	7	7
-Y180	4	2	3	1	7	7
Z180	6	6	6	6	8	8
I	5	5	5	5	9	9

Table A.1: Gate-dependent cumulative error types for different combinations of computational gates S (columns) and Pauli gates P (rows) labelled from 1 to 9. The errors are grouped to 9 types according to their strengths defined in Eq. A.2. It should be mentioned that in our implementation rotations around z-axis are realized by changing the rotating frame definition, i.e. changing the phases of subsequent pulses and potentially the observation. In this way, a 180° rotation and a -180° rotation around z-axis are the same. Therefore only Z180, which means a 180° rotation around z-axis, is listed here.

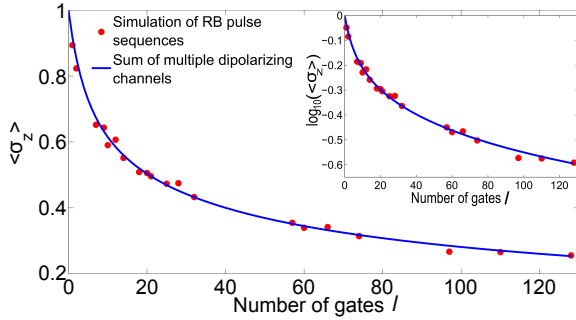


Figure A.12: Comparison between the numerically calculated prediction using Eq. A.5 (solid) and the realistic simulation averaged over 420 randomized benchmarking pulse sequences (\bullet). Excellent agreement between the two is observed. T_1 and T_2 processes are not taken into account.

pressed as [1]:

$$\hat{\Lambda}_{\epsilon,ave} = \sum_{i=1}^9 w_i \hat{\Lambda}_{\epsilon,ave,i}, \quad (\text{A.3})$$

$$p_\epsilon = \sum_{i=1}^9 w_i p_i. \quad (\text{A.4})$$

Here $\hat{\Lambda}_{\epsilon,ave,i}$ is the depolarized channel associated with the error type i with depolarizing parameter $p_i = (4 - |\text{Tr}(S P U_{inh}^\dagger)|^2)/3 = 4\xi_i/3$ [3]. w_i is the probability for the error type i to occur, and their values are $1/9, 1/9,$

$1/9, 1/9, 1/9, 1/9, 2/9, 1/18, 1/18.$

Finally, by averaging over the distribution of ϵ , the expression for the channel constructed from n random gates can be obtained as:

$$\hat{\Lambda}_{ave}(n) = \int d\epsilon g(\epsilon) \hat{\Lambda}_{\epsilon,ave}^n, \quad (\text{A.5})$$

where $\hat{\Lambda}_{\epsilon,ave}^n(\rho) = (1 - p_\epsilon)^n \rho$ and ρ is the deviation density matrix or the traceless part of the full density matrix. Therefore, the fidelity decay (in our case, the decay of the expectation value of σ_z) is the sum of multiple exponential decays weighted with the distribution function $g(\epsilon)$.

Using experimentally measured values for $g(\epsilon)$, we compare in Fig. A.12 the decay curve numerically calculated from Eq. A.5 with the curve obtained by simulating randomized benchmarking sequences. The evaluation of Eq. A.5 is carried out numerically since U_{inh} is generated by a time-dependent Hamiltonian with two non-commuting terms, σ_z term representing the off-resonance effect and $\sigma_{x,y}$ terms for the external control. For the S and P gates, 35 ns Gaussian pulses with 1 ns time steps are used. Two decay curves agree very well, indicating the T_2^* incoherent error is responsible for the non-exponential behavior of the fidelity decay. Furthermore, in the experimental data, the decay curve fits very well to a single-exponential function within the error bar when T_2^* is extended using the selection sequence (\square in Fig. 11). Therefore, we conclude that the non-exponential fidelity decay can be explained by the T_2^* error.

References

- [1] C. A. Ryan, M. Laforest, R. Laflamme, Randomized benchmarking of single- and multi-qubit control in liquid-state nmr quantum information processing, *New J. of Phys.* 11 (1) (2009) 013034.
- [2] C. Negrevergne, T. S. Mahesh, C. A. Ryan, M. Ditty, F. Cyr-Racine, W. Power, N. Boulant, T. Havel, D. G. Cory, R. Laflamme, Benchmarking quantum control methods on a 12-qubit system, *Physical Review Letters* 96 (17) (2006) 170501.
- [3] J. Emerson, R. Alicki, K. Zyczkowski, Scalable noise estimation with random unitary operators, *Journal of Optics B: Quantum and Semiclassical Optics* 7 (10) (2005) S347.
- [4] E. Knill, D. Leibfried, R. Reichle, J. Britton, R. B. Blakestad, J. D. Jost, C. Langer, R. Ozeri, S. Seidelin, D. J. Wineland, Randomized benchmarking of quantum gates, *Phys. Rev. A* 77 (2008) 012307.
- [5] C. Dankert, R. Cleve, J. Emerson, E. Livine, Exact and approximate unitary 2-designs and their application to fidelity estimation, *Physical Review A* 80 (1) (2009) 012304.
- [6] E. Magesan, J. M. Gambetta, J. Emerson, Scalable and robust randomized benchmarking of quantum processes, *Phys. Rev. Lett.* 106 (2011) 180504.

- [7] E. Magesan, J. M. Gambetta, J. Emerson, Characterizing quantum gates via randomized benchmarking, *Phys. Rev. A* 85 (2012) 042311.
- [8] E. Knill, R. Laflamme, Theory of quantum error-correcting codes, *Physical Review A* 55 (2) (1997) 900.
- [9] E. Knill, R. Laflamme, W. H. Zurek, Resilient quantum computation, *Science* 279 (5349) (1998) 342–345.
- [10] J. Preskill, Reliable quantum computers, *Proceedings of the Royal Society of London. Series A: Mathematical, Physical and Engineering Sciences* 454 (1969) (1998) 385–410.
- [11] E. Knill, Quantum computing with realistically noisy devices, *Nature* 434 (7029) (2005) 39–44.
- [12] P. Aliferis, D. Gottesman, J. Preskill, Accuracy threshold for postselected quantum computation, *Quantum Information & Computation* 8 (3) (2008) 181–244.
- [13] D. Gottesman, Stabilizer codes and quantum error correction. caltech ph. d, Ph.D. thesis, Thesis, eprint: quant-ph/9705052 (1997).
- [14] T. H. Taminiau, J. Cramer, T. van der Sar, V. V. Dobrovitski, R. Hanson, Universal control and error correction in multi-qubit spin registers in diamond, *Nature Nanotechnology* 9 (3) (2014) 171–176.
- [15] J. Kelly, R. Barends, A. G. Fowler, A. Megrant, E. Jeffrey, T. C. White, D. Sank, J. Y. Mutus, B. Campbell, Y. Chen, Z. Chen, B. Chiaro, A. Dunsworth, I. C. Hoi, C. Neill, P. J. J. O’Malley, C. Quintana, P. Roushan, A. Vainsencher, J. Wenner, A. N. Cleland, J. M. Martinis, State preservation by repetitive error detection in a superconducting quantum circuit, *Nature* 519 (7541) (2015) 66–69.
- [16] T. Maly, G. T. Debelouchina, V. S. Bajaj, K.-N. Hu, C.-G. Joo, M. L. Mak-Jurkauskas, J. R. Sirigiri, P. C. van der Wel, J. Herzfeld, R. J. Temkin, et al., Dynamic nuclear polarization at high magnetic fields, *The Journal of chemical physics* 128 (5) (2008) 052211.
- [17] A. B. Barnes, G. De Paepe, P. C. A. Van der Wel, K.-N. Hu, C.-G. Joo, V. S. Bajaj, M. L. Mak-Jurkauskas, J. R. Sirigiri, J. Herzfeld, R. J. Temkin, et al., High-field dynamic nuclear polarization for solid and solution biological nmr, *Applied magnetic resonance* 34 (3-4) (2008) 237–263.
- [18] S. Simmons, R. M. Brown, H. Riemann, N. V. Abrosimov, P. Becker, H.-J. Pohl, M. L. W. Thewalt, K. M. Itoh, J. J. L. Morton, Entanglement in a solid-state spin ensemble, *Nature* 470 (7332) (2011) 69–72.
- [19] V. Filidou, S. Simmons, S. D. Karlen, F. Giustino, H. L. Anderson, J. J. L. Morton, Ultrafast entangling gates between nuclear spins using photoexcited triplet states, *Nature Physics* 8 (8) (2012) 596–600.
- [20] L. J. Schulman, T. Mor, Y. Weinstein, Physical limits of heat-bath algorithmic cooling, *Physical Review Letters* 94 (2005) 120501.
- [21] J. Baugh, O. Moussa, C. A. Ryan, A. Nayak, R. Laflamme, Experimental implementation of heat-bath algorithmic cooling using solid-state nuclear magnetic resonance, *Nature* 438 (7067) (2005) 470–473.
- [22] C. A. Ryan, O. Moussa, J. Baugh, R. Laflamme, Spin based heat engine: Demonstration of multiple rounds of algorithmic cooling, *Physical Review Letters* 100 (2008) 140501.
- [23] D. K. Park, G. Feng, R. Rahimi, S. Labruyère, T. Shibata, S. Nakazawa, K. Sato, T. Takui, R. Laflamme, J. Baugh, Hyperfine spin qubits in irradiated malonic acid: heat-bath algorithmic cooling, *Quantum Information Processing* 14 (7) (2015) 2435–2461.
- [24] N. Khaneja, Switched control of electron nuclear spin systems, *Phys. Rev. A* 76 (2007) 032326.
- [25] J. S. Hodges, J. C. Yang, C. Ramanathan, D. G. Cory, Universal control of nuclear spins via anisotropic hyperfine interactions, *Physical Review A* 78 (1) (2008) 010303.
- [26] Y. Zhang, C. A. Ryan, R. Laflamme, J. Baugh, Coherent control of two nuclear spins using the anisotropic hyperfine interaction, *Physical review letters* 107 (17) (2011) 170503.
- [27] T. Borneman, Techniques for noise suppression and robust control in spin-based quantum information processors, Ph.D. thesis, Massachusetts Institute of Technology (2012).
- [28] N. Khaneja, T. Reiss, C. Kehlet, T. Schulte-Herbrüggen, S. J. Glaser, Optimal control of coupled spin dynamics: design of nmr pulse sequences by gradient ascent algorithms, *Journal of Magnetic Resonance* 172 (2) (2005) 296–305.
- [29] Y. Zhang, Universal control in $1e-2n$ spin system utilizing anisotropic hyperfine interactions, Master’s thesis, University of Waterloo (2010).
- [30] J. Chamilliard, On an electron spin resonance spectrometer for quantum information processing, Master’s thesis, University of Waterloo (2011).
- [31] W. Froncisz, T. Oles, J. S. Hyde, Qband loopgap resonator, *Review of Scientific Instruments* 57 (6) (1986) 1095–1099.
- [32] G. Rinard, G. Eaton, Loop-gap resonators, in: S. Eaton, G. Eaton, L. Berliner (Eds.), *Biomedical EPR, Part B: Methodology, Instrumentation, and Dynamics*, Vol. 24/B of *Biological Magnetic Resonance*, Springer US, 2005, pp. 19–52.
- [33] M. J. Biercuk, H. Uys, A. P. Vandevender, N. Shiga, W. M. Itano, J. J. Bollinger, High-fidelity quantum control using ion crystals in a penning trap, *Quantum Info. Comput.* 9 (11) (2009) 920–949.
- [34] K. R. Brown, A. C. Wilson, Y. Colombe, C. Ospelkaus, A. M. Meier, E. Knill, D. Leibfried, D. J. Wineland, Single-qubit-gate error below 10^{-4} in a trapped ion, *Phys. Rev. A* 84 (2011) 030303.
- [35] J. M. Chow, J. M. Gambetta, L. Tornberg, J. Koch, L. S. Bishop, A. A. Houck, B. R. Johnson, L. Frunzio, S. M. Girvin, R. J. Schoelkopf, Randomized benchmarking and process tomography for gate errors in a solid-state qubit, *Phys. Rev. Lett.* 102 (2009) 090502.
- [36] R. Barends, J. Kelly, A. Megrant, A. Veitia, D. Sank, E. Jeffrey, T. C. White, J. Mutus, A. G. Fowler, B. Campbell, Y. Chen, Z. Chen, B. Chiaro, A. Dunsworth, C. Neill, P. O’Malley, P. Roushan, A. Vainsencher, J. Wenner, A. N. Korotkov, A. N. Cleland, J. M. Martinis, Superconducting quantum circuits at the surface code threshold for fault tolerance, *Nature* 508 (7497) (2014) 500–503.
- [37] S. Olmschenk, R. R. Chircireanu, K. D. Nelson, J. Porto, Randomized benchmarking of atomic qubits in an optical lattice, *New Journal of Physics* 12 (11) (2010) 113007.
- [38] J. T. Muhonen, A. Laucht, S. Simmons, J. P. Dehollain, R. Kalra, F. E. Hudson, S. Freer, K. M. Itoh, D. N. Jamieson, J. C. McCallum, A. S. Dzurak, A. Morello, Quantifying the quantum gate fidelity of single-atom spin qubits in silicon by randomized benchmarking, *Journal of Physics: Condensed Matter* 27 (15) (2015) 154205.
- [39] S. Bravyi, A. Kitaev, Universal quantum computation with ideal clifford gates and noisy ancillas, *Phys. Rev. A* 71 (2005) 022316.
- [40] M. Laforest, Error characterization and quantum control benchmarking in liquid state nmr using quantum information processing techniques, Ph.D. thesis, University of Waterloo (2008).
- [41] C. C. López, B. Lévi, D. G. Cory, Error characterization in quantum information processing: A protocol for analyzing spatial correlations and its experimental implementation, *Phys. Rev. A* 79 (2009) 042328.
- [42] S. Eaton, G. Eaton, Irradiated fused-quartz standard sample for time-domain epr, *Journal of Magnetic Resonance, Series A* 102 (3) (1993) 354 – 356.

- [43] M. H. Levitt, *Composite Pulses*, John Wiley & Sons, Ltd, 2007.
- [44] R. Tycko, Broadband population inversion, *Phys. Rev. Lett.* 51 (1983) 775–777.
- [45] D. Cory, A dante-based method for radiofrequency-field selection, *Journal of Magnetic Resonance, Series A* 103 (1) (1993) 23 – 26.
- [46] A. Shaka, J. Keeler, M. Smith, R. Freeman, Spatial localization of nmr signals in an inhomogeneous radiofrequency field, *Journal of Magnetic Resonance* (1969) 61 (1) (1985) 175 – 180.
- [47] M. A. Pravia, N. Boulant, J. Emerson, A. Farid, E. M. Fortunato, T. F. Havel, R. Martinez, D. G. Cory, Robust control of quantum information, *The Journal of Chemical Physics* 119 (19) (2003) 9993–10001.
- [48] N. Boulant, J. Emerson, T. F. Havel, D. G. Cory, S. Furuta, Incoherent noise and quantum information processing, *The Journal of Chemical Physics* 121 (7) (2004) 2955–2961.
- [49] C. A. Ryan, M. Laforest, R. Laflamme, Randomized benchmarking of single-and multi-qubit control in liquid-state NMR quantum information processing, *New Journal of Physics* 11 (1) (2009) 013034.